Electronic Supplementary Information (ESI) for Chemical Communications This journal is (c) The Royal Society of Chemistry 2025

Versatile 1D structured Co_3O_4–Co/NC@N–carbon nanotubes for high-performance lithium storage

Linan Yang,[a,1] Chengjie Zhang,[a,1] Liuyang Cao,[a,1] Hongjin Li,[a] Hongbo Li,[b] Zhanjun Yang,[a,*] Juan Li[a,*]

[a] *School of Chemistry and Chemical Engineering, Yangzhou University, Yangzhou 225002, P.R. China*

[b] *School of Chemistry and Chemical Engineering, Yancheng Institute of Technology, Yancheng 224051, P. R. China.*

Experimental

Materials and Reagents. All of the electrolytes and Whatman glass fiber (GF/D) were sourced from DodoChem Co., Ltd. Ferric chloride hexahydrate ($FeCl_3 \cdot 6H_2O$), cobaltous nitrate hexahydrate ($Co(NO_3)_2 \cdot 6H_2O$), 2-methylimidazole (2-MI), methyl orange, pyrrole monomer, metallic lithium foil, N-Methyl-2-pyrrolidone (NMP), methanol, ethanol, polyvinylidene fluoride (PVDF) and acetylene black were purchased from Shanghai Sinopharm Co., Ltd. No further processing is applied to any of the chemicals.

Instruments. Scanning electron microscopy (SEM, Zeiss-Supra 55) and transmission electron microscopy (TEM, JEM-2100) were used to observe the structure and size of the materials. High-resolution transmission electron microscopy (HRTEM, Tecnai G2 F30 S-TWIN) was used to further obtain the internal structure details and element distribution information of the material. Polycrystalline powder X-ray diffractometer (XRD, D8 Advance) and Raman spectroscopy (Renishaw, Renishaw In Via, excitation wavelength 532 nm) were used to characterize the crystalline structure and properties of the materials. X-ray photoelectron spectroscopy (XPS, ThermoFisher

Scientific ESCALAB250Xi) was used to characterize the elemental composition, chemical and electronic states of the materials. The thermogravimetric analysis analyzer (Pyris 1 TGA) was used to measure the content of each component in the material, and the heating rate was 10 °C min^{-1}, in the temperature range of room temperature to 800°C. The specific surface area and pore structure of the materials were analyzed by N_2 absorption/desorption analyzer (Micromeritics ASAP 2020).

Preparation of nitrogen-doped carbon nanotubes (NCNTs). 0.082 g methyl orange and 0.676 g $FeCl_3 \cdot 6H_2O$ were dissolved in 25 mL deionized water, respectively, and a uniform solution was prepared by ultrasonic dispersion. The two solutions were mixed and stirred in an ice bath. Then 115 μL pyrrole monomer was slowly added and stirred at 0°C for 12 h. After the reaction, the black precipitate was centrifugally washed with ethanol and deionized water several times, and the product was dried overnight in the vacuum oven at 60°C. Finally, the obtained product was heated in a tube furnace at a rate of at 5 °C min^{-1} to 700°C in an Ar atmosphere and maintained at this temperature for 2 h to prepare NCNTs.

Preparation of ZIF–67@NCNTs and 1D structured Co_3O_4–Co/NC@NCNTs composite materials. The NCNTs prepared above were added to 20 mL methanol, and dispersed uniformly by ultrasound. And then 0.086 g Co $(NO_3)_2 \cdot 6H_2O$ was added and stirred for 1 h to obtain solution A. Subsequently, 0.685 g 2-MI was added to 20 mL methanol, and a uniform solution B was obtained by ultrasound. Next, solution B was slowly added to solution A. After reaction for 3 h under stirring conditions, then it was left to stand for 24 h. Finally, the ZIF–67@NCNTs composite was centrifuged with ethanol for several times and dried overnight at 60°C in the vacuum oven. The ZIF–67@NCNTs composite prepared in the previous step was heat treated in argon atmosphere of 550°C for 2 h to obtain the final 1D structured Co_3O_4–Co/NC@NCNTs with the heating rate of 2 °C min^{-1}.

Electrochemical measurements. The prepared electrode materials, acetylene black and PVDF were mixed according to the mass ratio of 7:2:1, and the solvent NMP was added and stirred magnetically for 8 h to prepare the slurry. The prepared slurry was evenly coated on the Cu foil and kept at 120°C in the vacuum oven for 12 h. After coating, they are cut into a circular electrode sheet with a diameter of 1.6 cm. Finally, the electrodes were weighed and the average load of active substances in the electrodes was 1.22 mg cm^{-2}. The model 2032 batteries were assembled in a glove box filled with Ar, and then left to rest for 12 h after assembly. Xinwei battery test system was used to test the constant current charge and discharge of the battery. Under different current density test conditions, the battery rate performance was studied by charge/ discharge test, and the cycle stability was observed by 100 and 500 cycles at 0.1 A g^{-1} and 1.0 A g^{-1} current density, respectively. The cyclic voltammetry (CV) tests were carried out with Chenhua electrochemistry workstation, and the test voltage ranges were set to 0.01–3 V, and the scanning speed was set to 0.2–1.0 mV s^{-1}. And the electrochemical impedance spectroscopy (EIS) tests were also carried out in the electrochemical workstation, and the scanning frequency was 0.01 Hz–100 KHz.

The morphology of PPy.

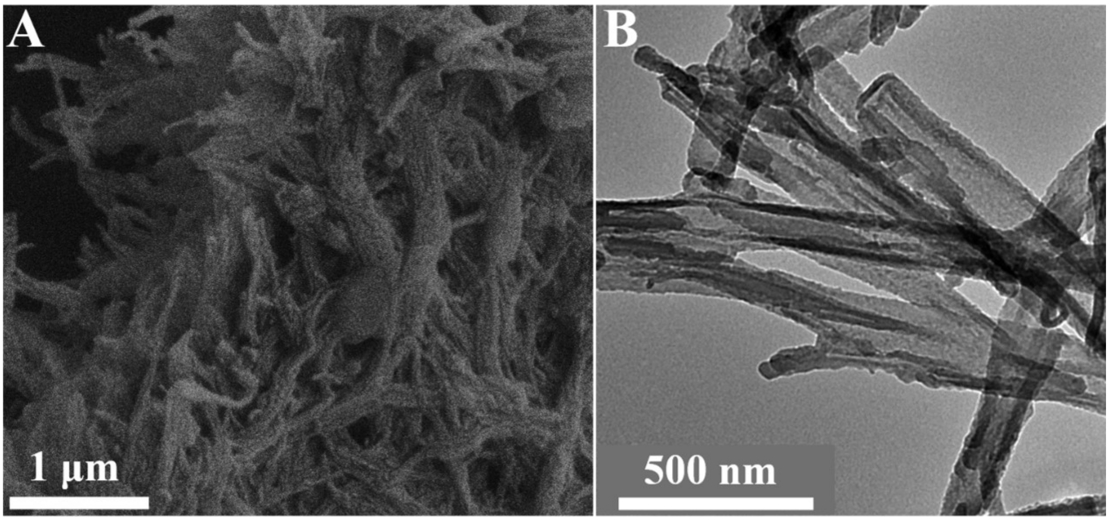

Figure S1. (A) SEM and (B) TEM images of the PPy.

N_2 isothermal adsorption/desorption measurements of NCNTs, ZIF-67@NCNTs and Co_3O_4–Co/NC@NCNTs composite and thermogravimetric analysis of 1D structured Co_3O_4–Co/NC@NCNTs composite materials.

Through the N_2 adsorption/desorption tests, the specific surface area of NCNTs is 63.89 m^2/g. And there are many macropore (>50 nm) in NCNTs through the pore size distribution curve (Fig. S2A). ZIF-67@NCNTs has a specific surface area of 1162.95 m^2/g, and the adsorption isotherms conform to the characteristics of Type I, which indicates that is a microporous material (Fig. S2B). The high surface area and the main micropores may also lead to some side reactions, such as the reduction decomposition of the electrolyte and the formation of the solid electrolyte interface layer, which results in a larger initial irreversible capacity loss and a lower coulomb efficiency. However, Co_3O_4–Co/NC@NCNTs composite materials (Fig. S2C) have more mesoporous structure than the two compared materials. This can be due to the fact that a large amount of gas was produced during the pyrolysis process, resulting in the formation of a large number of mesoporous structures inside the composite material. The increased mesoporous structure can enhance the wettability and contact area of the electrolyte, accelerate Li^+ diffusion and electron transport. Meanwhile, such a structure can alleviate volume expansion, improve the stability of the electrode structure, and thereby achieve good electrochemical performance.

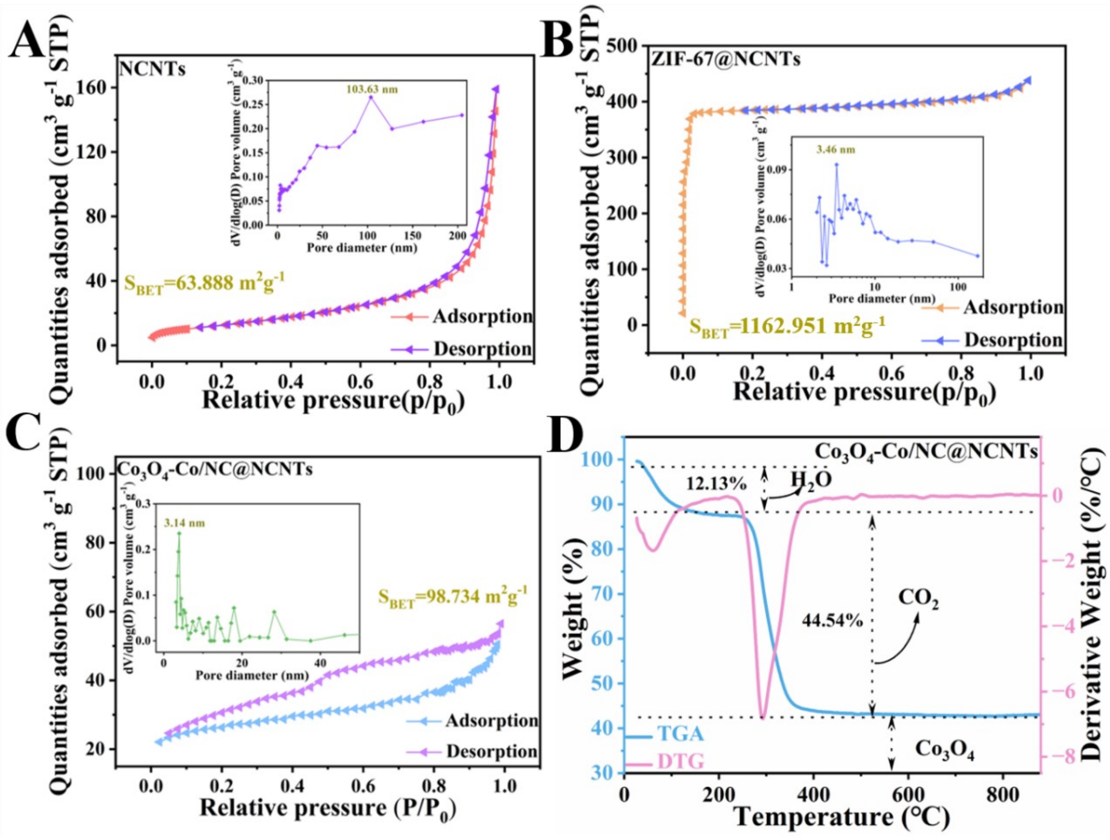

Figure S2. (A-C) N_2 adsorption-desorption isotherm, inset is pore size distribution curve of NCNTs, ZIF-67@NCNTs and Co_3O_4–Co/NC@NCNTs composite. (D) TG curve of Co_3O_4–Co/NC@NCNTs composite.

X-ray photoelectron spectra of 1D structured Co_3O_4–Co/NC@NCNTs composite materials.

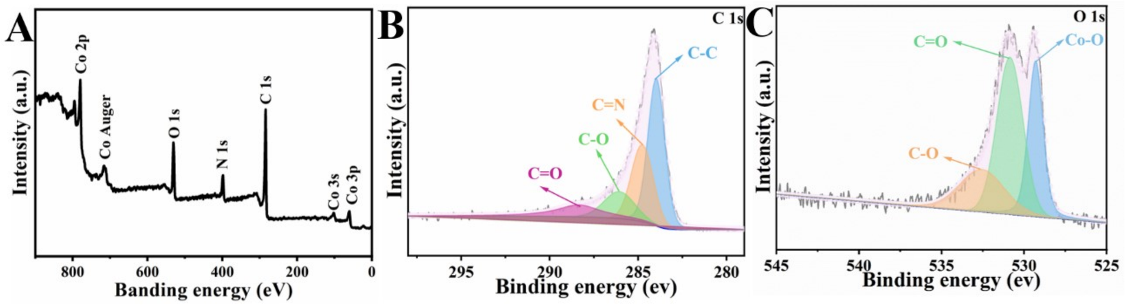

Figure S3. X-ray photoelectron spectra of Co_3O_4–Co/NC@NCNTs composite: (A) full spectra, high resolution (B) C 1s and (C) O 1s.

Lithium storage mechanism discussion.

In order to explore the possible reasons for enhancing cyclic stability and rate performance of the Co_3O_4–Co/NC@NCNTs electrode, CV tests were performed at a series of scan rates of 0.2-1.0 mV s^{-1} (Fig. S4A) to investigate the electrochemical kinetics and lithium storage mechanism of the electrode[S1]. The results show that CV curves show similar shape at different scanning rates, and oxidation potential shifted positively with the increase of scanning rate, and the peak intensity of redox increased gradually. In general, the total charge stored while cycling in the electrochemical energy storage device is related to several mechanisms. It can be characterized according to formula (1) and (2) and CV data at different scan rates:

$$i = av^b \#(1)$$

$$\log(i) = b\log(v) + \log(a) \#(2)$$

Where i represents the current density, v represents the sweep rate, and a and b are constants. The charge storage mechanism is closely related to b value. When b value is close to 0.5, the charge storage process is dominated by diffusion control process. On the contrary, when b value approaches 1.0, it is mainly controlled by capacitive behavior. In Fig. S4B, it can be seen that the b values of Co_3O_4–Co/NC@NCNTs from the cathode peak and the anode peak are 0.86 and 0.82, respectively, indicating that both diffusion and capacitance control contribute to the capacity during the cycle. The ratio of capacitance to diffusion contribution can be obtained by formula (3):

$$i(v) = k_1 v + k_2 v^{\frac{1}{2}} \#(3)$$

Among them, $k_1 v$ and $k_2 v^{1/2}$ are the contributions of pseudocapacitance control process and diffusion control process, respectively. The distribution of capacitive charge at a scanning rate of 1.0 mV s^{-1} is fitted in Fig. S4C, where the pseudocapacitance contribution of the blue part is 76.1%. As shown in Fig. S4D as the scan rate increases, so does the proportion of capacitance contribution. When the scan rate changes from 0.2 to 1.0 mV s^{-1}, the capacitive contribution increases from 59% to 76%. The high capacitive behavior contribution ratio means that the fast insertion/extraction of Li^+ of Co_3O_4–Co/NC@NCNTs helps to achieve superior rate capability and long-term cycle stability at high current density.

To study the electrochemical reaction kinetics of the electrodes, electrochemical impedance spectroscopy (EIS) analysis was performed in Fig. S4E. In general, the ohmic resistance of the battery is related to the intercept value of the Z' axis semicircle at the high intermediate frequency, while the low-frequency sloping line corresponds to the diffusion of Li^+ in the electrode[S2]. The resistance of Co_3O_4–Co/NC@NCNTs electrode is lower than that of NCNTs and ZIF-67@NCNTs electrodes, indicating that the Co_3O_4-Co/NC@NCNTs has better conductivity and faster charge transfer kinetics. In order to further clarify the diffusion kinetics of Li^+ in the electrode material, the Z'-$\omega^{1/2}$ in the low frequency region of the EIS curve was fitted according to the formula $Z' = R_e + R_{ct} + \sigma\omega^{-1/2}$ and the corresponding fitting calculation was performed (Fig. S4F). The fitting results can be estimated by the formula $D_{Li^+} = R^2T^2/2n^4F^4C^2\sigma^2A^2$, that is, the diffusion rate of Li^+ is inversely proportional to the slope of the sloping line in Fig. S4F. The slope of the electrodes of NCNTs, ZIF–67@NCNTs and Co_3O_4–Co/NC@NCNTs by fitting calculation are 114.1, 113.9 and 27.3, respectively. It is shown that the Co_3O_4–Co/NC@NCNTs electrode has the smallest slope, which proves that it has the fastest Li^+ diffusion kinetics, and thus improves the electrochemical reaction kinetics and rate performance.

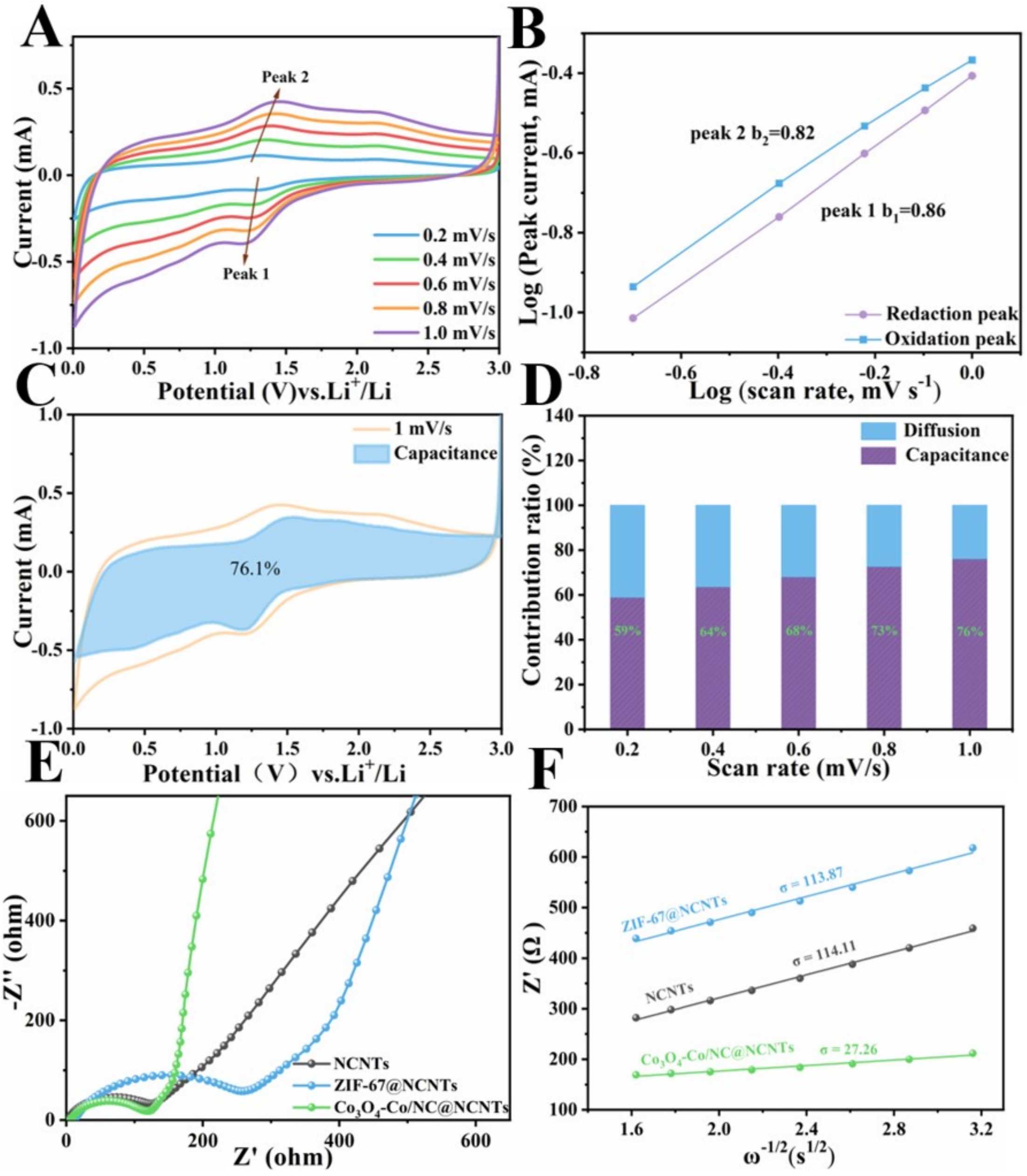

Figure S4. (A) CV curves at different sweep rates for the Co_3O_4–Co/NC@NCNTs electrode. (B) Fitted log (peak current) vs log (sweep rate) corresponding to certain electrochemical reactions. (C) The CV curve at a sweep rate of 1 mV s^{-1} marking the pseudocapacity contribution (blue region) in comparison to the total current. (D) Capacity contribution at various sweep rates. (E) Nyquist plots of the NCNTs, ZIF–67@NCNTs and Co_3O_4–Co/NC@NCNTs electrodes. (F) Real parts of the complex impedances vs. $\omega^{-1/2}$ (angular frequency).

Table S1 Comparison of lithium storage performance of some Co-based anode materials.

Sample	Current density ($A\ g^{-1}$)	Number of cycles	Capacity ($mAh\ g^{-1}$)	Synthesis complexity	Stability	Cost	Reference
Cry–Co_3O_4/Co@N–C–700	0.2	50	617.4	medium	low	low	3
Co–MOFs/rGO	0.1	500	692.25	medium	medium	high	4
Co/Co_3O_4–C	0.5	200	608	high	high	high	5
CoSe/Co@NC	0.2	100	630	medium	low	low	6
ES–CNCo_3O_4	1	700	647	high	high	high	7
G/Co_3O_4	0.2	200	714	medium	low	medium	8
Co_9S_8/C–CNFs	0.5	150	700	low	low	low	9
Co_3O_4/NPC	0.5	300	785	high	high	high	10
Co_3O_4–Co/NC@NCNTs	0.1	100	809.4	low	high	low	This article
	1	500	663.6				

Note: *Cry–Co_3O_4/Co@N–C–700* (Crystalline–Co_3O_4/Co@N-doped carbon–700), *Co–MOFs/rGO* (Co–MOFs/graphene oxide composite), *Co/Co_3O_4–C* (porous Co/Co_3O_4–C core-branch nanowire arrays), *CoSe/Co@NC* (CoSe/Co nanoparticles wrapped in layered carbon nitride nanosheets), *ES–CNCo_3O_4* (electrospinning of ZIF–67 NPs followed by a thermal treatment), *G/Co_3O_4* (Graphene-supported ultrafine Co_3O_4 nanocrystallites oxides), *Co_9S_8/C–CNFs* (Co_9S_8/carbonized cellulose nanofibers), *Co_3O_4/NPC* (Co_3O_4 nanoparticles on N-doped porous carbon).

References

S1 J. Li, D. Yan, X. Zhang, S. Hou, T. Lu, Y. Yao, L. Pan, *J. Mater. Chem. A* 2017, **5**, 20428.

S2 Y. Zhao, J. Wang, C. Ma, L. Cao, Z. Shao, *Chem. Eng. J.* 2019, **370**, 536-546.

S3 S. Guo, J. Liu, Q. Zhang, Y. Jin, H. Wang, *J. Alloys Compd.* 2021, **855**, 157538.

S4 X. Lang, X. Wang, Y. Liu, K. Cai, L. Li, Q. Zhang, *Int. J. Energy Res.* 2021, **45**, 4811–4820.

S5 G. Pan, X. Xia, F. Cao, J. Chen, Y. Zhang, *J. Power Sources* 2015, **293**, 585–591.

S6 Y. Zhou, R. Tian, H. Duan, K. Wang, Y. Guo, H. Li, H. Liu, *J. Power Sources*, 2018, **399**, 223–230.

S7 C. Zhang, B. Lu, F. Cao, Z. Yu, H. Cong, S. Yu, *J. Mater. Chem. A*, 2018, **6**, 12962–12968.

S8 Q. Qu, T. Gao, H. Zheng, X. Li, H. Liu, M. Shen, J. Shao, H. Zheng, *Carbon*, 2015, **92**, 119–125.

S9 S. Guo, P. Zhang, Y. Feng, Z. Wang, X. Li, J. Yao, *J. Alloys Compd.* 2020, **818**, 152911.

S10 G. Zhuang, Y. Gao, X. Zhou, X. Tao, J. Luo, Y. Gao, Y. Yan, P. Gao, X. Zhong, J. Wang, *Chem. Eng. J.* 2017, **330**, 1255–1264.